Comparison of Simulated Plasma Flowfields to Experimental Measurements for a Gas-Fed Magnetoplasmadynamic Thruster

K. Sankaran[*], **S.C. Jardin**[†] and **E.Y. Choueiri**[‡]
Princeton University, Princeton, New Jersey 08544

AIAA-03-4843[§]

22^{nd} July, 2003

Abstract

The flowfield of a magnetoplasmadynamic thruster was simulated numerically and the results compared to experimental measurements, in order to validate the code and obtain insight into underlying physical processes. The thruster chosen was the full-scale benchmark thruster, because it has been the subject of many experimental studies. The parallelized axi-symmetric code featured detailed physical models and a finite volume formulation that allowed for non-orthogonal grids. Flowfield properties, such as electron density, velocity, current density, electron temperature, ionization fraction, mass and momentum flux, as well as thrust, compared favorably with existing data. The simulation provided insight into some aspects of thruster operation, such as the weak role of the anode geometry in affecting the thrust, the predominantly electromagnetic nature of the thrust at nominal operating conditions, and the importance of the near cathode region in energy dissipation.

Nomenclature

ρ	Total mass density
$\mathbf{u}$	Fluid velocity
$\mathbf{B}$	Magnetic induction
$p, \bar{\bar{p}}$	Gas pressure, isotropic pressure tensor
E	Electric field strength
E'	Electric field seen by the plasma
$\mathcal{E}$	Energy density of the plasma
$\mathbf{j}$	Current per unit area
k_B	Boltzmann's constant
$k_{e,i}$	Electron/ion thermal conduction coefficient
m_e	Mass of an electron
p_h, p_e	Heavy species/electron pressure
T_h, T_e	Heavy species/electron temperature
η	Resistivity

1 Introduction

The Princeton full-scale benchmark thruster (FSBT) is a magnetoplasmadynamic thruster (MPDT) that has been the subject of many experimental investigations [1, 2, 3, 4, 5, 6, 7, 8, 9] over the past three decades. Yet, there has not been a detailed numerical simulation of this device. Now, with the improvements in numerical methods[10, 11] and computing capability[12], it is insightful to revisit this device, by comparing experimental measurements to results from a recently developed code[12].

Another goal of this comparison is to validate this code for future use with thrusters for which experimental data are not yet widely available, such as the lithium Lorentz force accelerator (LiLFA)[13].

[*] Ph.D. candidate

[†] Principal Research Scientist, Princeton Plasma Physics Lab; Professor, Astrophysical Sciences Dept.

[‡] Chief Scientist at EPPDyL. Associate Professor, MAE Dept.; Associate Fellow of AIAA.

[§] Presented at the 39^{th} AIAA/ASME/SAE/ASEE Joint Propulsion Conference, 20-23^{rd} July, 2003, Huntsville, AL.

In §2, we describe the governing equations and the physical models used in this simulation. Then, in §3 we describe how these equations were formulated to be solved in a non-orthogonal coordinate system in a conservative fashion. In §4 we discuss the discretization method and the boundary conditions imposed on the solver to calculate the flowfield in self-field magnetoplasmadynamic thrusters (MPDTs). In §5 we present the results from the simulation of plasma flows in the FSBT, and compare the results to experimental measurements. In §6 we use these aforementioned results to investigate some underlying physical processes in the FSBT.

2 Physical Model

The governing equations for a MHD flow problem can be written in the form [10]:

$$\frac{\partial}{\partial t}\begin{bmatrix}\rho\\ \rho\mathbf{u}\\ \mathbf{B}\\ \mathcal{E}\end{bmatrix}+\nabla\cdot\begin{bmatrix}\rho\mathbf{u}\\ \rho\mathbf{uu}+\bar{\bar{p}}-\bar{\bar{\mathcal{B}}}_M\\ \mathbf{uB}-\mathbf{Bu}\\ (\mathcal{E}+p)\,\mathbf{u}-\bar{\bar{\mathcal{B}}}_M\cdot\mathbf{u}\end{bmatrix}=\mathbf{D}. \quad (1)$$

The right hand side of the equation, $\mathbf{D}$, contains the dissipative effects that are physical in nature, and they too are written as divergence of fluxes, as seen in appendix A.

In the momentum equation, $\bar{\bar{\mathcal{B}}}_M=\frac{1}{\mu_o}\left[\mathbf{BB}-\frac{B^2}{2}\mathbf{I}\right]$ is the magnetic part of the Maxwell stress tensor, and it satisfies the relation,

$$\nabla\cdot\bar{\bar{\mathcal{B}}}_M=\mathbf{j}\times\mathbf{B}\,. \quad (2)$$

In Faraday's law, the contribution of back EMF to the change in magnetic field is written as a divergence of a flux,

$$-\nabla\times(\mathbf{u}\times\mathbf{B})=\nabla\cdot(\mathbf{uB}-\mathbf{Bu})\ . \quad (3)$$

The energy equation is written in terms of the energy density (energy per unit volume), $\mathcal{E}$, which includes the internal energy, kinetic energy and the energy in the magnetic field. The dissipative flux of energy, $\nabla\cdot\mathbf{q}$, contains the Ohmic heating (written in terms of divergence of the Poynting flux), and thermal conduction,

$$\nabla\cdot\mathbf{q}=\nabla\cdot\left[\frac{\mathbf{B}\times\mathbf{E}'}{\mu_0}+\bar{\bar{k}}_{th}\cdot\nabla T\right]\ .$$

In addition to the total energy equation, we needed to account for the disparity between electron and ion temperatures. The conservation relations for the internal energy density of electrons, $\mathcal{E}_e$, can be written as

$$\frac{\partial\mathcal{E}_e}{\partial t}+\nabla\cdot[\mathcal{E}_e\mathbf{u}]+p_e\nabla\cdot\mathbf{u}=\eta j^2-\Delta\dot{\mathcal{E}}_{ie}+\nabla\cdot(k_e\nabla T_e)\ . \quad (4)$$

In the above expression, ηj^2 is the Ohmic heating term. The rate of exchange of energy per unit volume between the electrons and the ions, through collisions, $\Delta\dot{\mathcal{E}}_{ie}$, is

$$\Delta\dot{\mathcal{E}}_{ie}=\frac{3\rho_e\nu_{ei}}{M_i}k_B\left(T_e-T_i\right)\ , \quad (5)$$

where ρ_e is the electron mass density, and ν_{ei} is the average collision frequency between electrons and ions.

The internal energy of ions can be obtained by subtracting electron internal energy from the total internal energy.

2.1 Transport Phenomena

The transport phenomena included in our model are electron and ion thermal conduction, classical electrical resistivity with Hall effect, and anomalous transport[14] due to momentum exchange between particles in the plasma and waves induced by current-driven microinstabilities in a collisional and finite-β magnetized plasma[15]. Details of incorporating these phenomena into this code are given in ref.[12].

2.2 Equation of State

For argon, the ideal gas model is not accurate for temperatures greater than 0.5 eV. As energy is deposited into internal modes, the ratio of specific heats deviates significantly from the ideal value of 5/3. Moreover, the relationship between pressure and temperature is nonlinear. Our equation-of-state model uses the partition function to compute the ratio

of specific heats, and the relationship between pressure and temperature. Details of this are provided in ref.[12].

2.3 Ionization

The plasma in a self-field, quasi-steady MPDT is generally in a state of ionizational nonequilibrium [16]. Though some numerical simulations (such as refs.[17]) have used finite-rate ionization models, they do not include higher levels of ionization that have been observed experimentally [18, 19]. In the present work, like in refs.[20, 21], we use a multi-level equilibrium ionization model. The details of the ionization model, including the energy levels, are provided in ref.[12].

3 Finite Volume Formulation

The MHD equations in eqn.(1) are conservation relations for mass *density*, momentum *density*, magnetic flux, and energy *density*. However, in reality, the conserved quantities are, mass, momentum, magnetic flux, and energy. Therefore, the first, second, and the fourth equations in the set eqn.(1) need to be multiplied by the volume of the cell.
Equations of the form

$$\frac{\partial U}{\partial t} = \frac{\partial f}{\partial r} + \frac{\partial g}{\partial z} + S, \tag{6}$$

upon multiplication by the cell volume ($2\pi r dr dz$) take the form,

$$\frac{\partial (rU)}{\partial t} = \frac{\partial (rf)}{\partial r} + \frac{\partial (rg)}{\partial z} + (S - f)\,. \tag{7}$$

The expanded form of these equations is given in the appendix A.

3.1 Integral Form

Equations of the type eqn.(7) can be written in their integral form. Every one of these conservation laws (for mass, radial momentum, axial momentum, magnetic flux, and total energy) can be individually written as:

$$\iint\limits_A \left[\frac{\partial U}{\partial t} = \left(\frac{\partial Fr}{\partial r} + \frac{\partial Fz}{\partial z} \right) + \text{Source} \right] dA\,. \tag{8}$$

The first term on the R.H.S. can be expressed as the curl of a vector, $\hat{\mathbf{F}} = [Fz, -Fr]$, because,

$$\nabla \times \hat{\mathbf{F}}|_\theta = \frac{\partial \hat{F}_r}{\partial z} - \frac{\partial \hat{F}_z}{\partial r} = \frac{\partial Fr}{\partial r} + \frac{\partial Fz}{\partial z}\,. \tag{9}$$

Using Stokes' theorem, this curl over the cell area can be expressed as the line integral around the edges of the cell,

$$\iint\limits_A \frac{\partial U}{\partial t} dA = \oint \hat{\mathbf{F}} \cdot \mathbf{dl} + \iint\limits_A (\text{Source})\, dA\,. \tag{10}$$

Since this equation is true irrespective of the shape of the control volume, the fluxes, *Fr* and *Fz*, can be written in the (*r,z*) coordinate system, as in the appendix A, regardless of the shape of the cell. This is a fundamental advantage of the finite-volume formulation over the finite-difference formulation, in addition to maintaining conservation.

4 Numerical Solution

The techniques for the numerical solution of eqns.(1-4) are described in ref.[10], and in this section we will only discuss how they are used to obtain solution for the flowfield in a self-field MPDT.

4.1 Spatial Discretization

Mathematically, the governing equations (eqns.(1-4)) are mixed hyperbolic and parabolic partial differential equations. The discretization scheme for the hyperbolic (convective) part of the problem involves using the characteristics to estimate fluxes through the cell surfaces, and is described in [10].

Unlike convective fluxes, dissipative fluxes depend upon gradients, and we need to compute derivatives across the surfaces for estimating $j_r, j_z, \partial T/\partial r$, and $\partial T/\partial z$. In an orthogonal grid system, we can estimate gradients by simply differencing the values in adjacent cells. However, in a non-orthogonal grid,

the adjacent cells/points are *not* along the lines of constant "*r*", or "*z*". So, here we have to estimate gradients in a different manner. This involves using the Stokes' theorem, and this method is described in appendix B.

4.2 Boundary Conditions

The method used for estimation of the convective and dissipative terms at various boundaries has remained the same as in ref.[12], where the details are found. Here, we will focus on the boundary between the plasma and the insulator.

Since all the enclosed current is downstream of the insulator (backplate, plus chamber inner in Fig.1), the stream function, $\psi = rB_\theta = \mu_o J_{tot}/2\pi$ is a constant at any given time at this boundary, and it depends only on the total current.

The electric field along the backplate, required for Faraday's law, is then

$$E_r(r,0) = E_r(r,\Delta z) + \Delta z \left(\frac{1}{r}\frac{\partial \psi}{\partial t} - \frac{\partial E_z}{\partial r} \right), \tag{11}$$

and the electric field along the chamber inner wall is

$$E_z(R_{ch},z) = E_z(R_{ch}-\Delta r,z) + \Delta r \left(\frac{1}{r}\frac{\partial \psi}{\partial t} + \frac{\partial E_r}{\partial z} \right). \tag{12}$$

At the inlet, a specified mass flow rate of propellant enters at a specified temperature at sonic conditions. In reality, the propellant is injected as neutral gas at room temperature, and it gets almost fully ionized within a few millimeters from the inlet[19]. However, it is believed[22] that this ionization process cannot be modeled by fluid theory. Therefore, in this model, the inlet temperature is chosen to be high enough such that the propellant is sufficiently ionized near the backplate.

5 MPDT Simulation Results

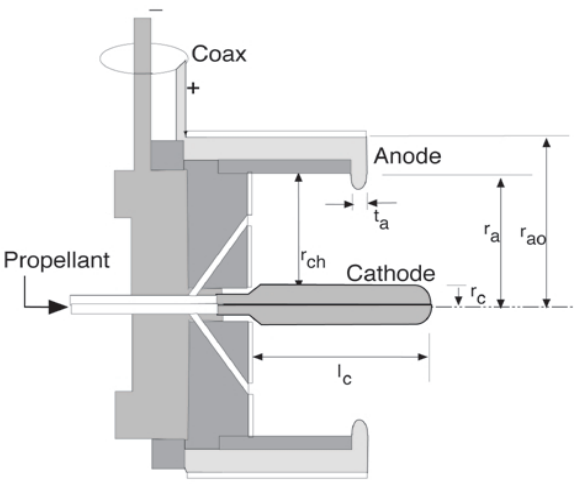

Figure 1: Princeton full-scale benchmark thruster, where r_c= 0.95 cm, r_a= 5.1 cm, r_{ao}=10.2 cm, r_{ch}= 6.4 cm, t_a= 0.95 cm, and l_c= 10.0 cm.

The geometry chosen for this simulation was the Princeton full-scale benchmark thruster[9]. It was chosen because of extensive experimental work that has been done on it[1, 5]. The relevant dimensions are given in Fig.1. In this paper, we only consider a propellant mass flow rate of 6.0 g/s of argon, and a total current of 16.0 kA, which corresponds to the nominal operating condition of ξ=1.0[23].

Note that in the simulation the thruster contains four mass injection ports - one at the base of the cathode (as in Fig.1) at a 45^o angle, and three others r = .2cm, 3 cm, and 4 cm through the backplate directed normally into the chamber. The version in Fig.1 has only one port through the backplate. For simplicity, the rounded corners of the anode lip and the cathode were truncated in the simulation.

The code described in this article solves the governing equations in a time-dependent manner. Therefore, in order to verify convergence, we monitored the time-dependent change (see eqn.(1)). The criteria we used was $\Delta t(\nabla \cdot F) \leq 10^{-7}$ (see Fig.2), and it was reached roughly at 300μs. The sudden change around t=50μs is because we changed the dJ/dt value at that point.

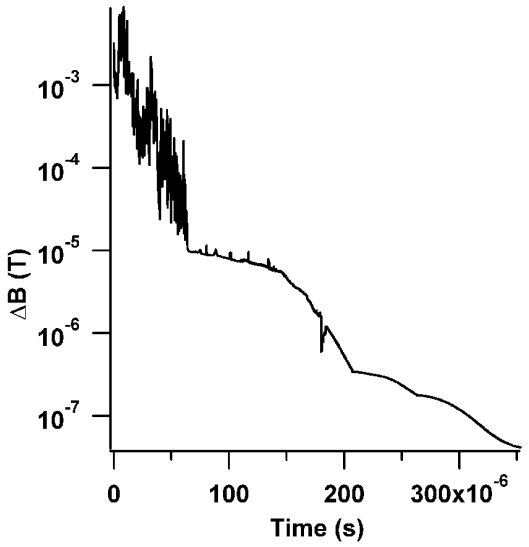

Figure 2: Convergence history: change in magnetic field vs. time.

We now present some of the results of the simulation. Unless explicitly stated otherwise, comparisons are made with measurements on a FSBT at J = 16 kA, and argon $\dot{m}$ = 6.0 g/s.

5.1 Density

The electron number density contours within the chamber are shown in Fig.11, where we note that, inside the chamber, n_e increases towards the cathode. This is attributed to the action of the radial pumping force, $j_z B_\theta$, which pushes the plasma towards the cathode. This trend has been observed in experiments and in previous simulations[17]. The density in the thruster chamber ranges from $\simeq 2.0\times10^{20}\mathrm{m}^{-3}$ near the chamber wall to $\simeq 5.0 \times 10^{21}\mathrm{m}^{-3}$ near the cathode. Outside the chamber, on the centerline near the cathode, one also finds a region of high density ($\simeq 5.0 \times 10^{21}\mathrm{m}^{-3}$), which is often termed as "cathode jet"[24]. In this simulation, the highest density, $\simeq 2.0 \times 10^{22}\mathrm{m}^{-3}$, is found near the injection port on the base of the cathode. While there exist no detailed measurements of electron density in the FSBT, Turchi[24] measured them for a similar geometry (dubbed as "Configuration A") with a shorter cathode. As reported in ref.[24], electron number densities near the cathode in the chamber, and on the centerline in front of the cathode are indeed around $\simeq 5.0 \times 10^{21}\mathrm{m}^{-3}$ and are in accordance with the results of the simulation.

5.2 Velocities

The contours of axial velocity are shown in Fig.12. The range of values (8.0 to 13.0 km/s) is in the range of measured values of local velocities reported in ref.[25] for these conditions. On the centerline, Boyle[26] measured axial velocity increasing from 10 km/s to 13 km/s, with distance from 2 cm to 15 cm in front of the cathode. It can be seen that this simulation also predicts a similar pattern and values.

5.3 Current

The calculated contours of enclosed current are shown in Fig.13. Unfortunately, the closest condition for which current contours are available for the FSBT is for J = 23.5 kA[3], and those contours are shown in Fig.4. In Fig.3, the calculated values are scaled to facilitate comparison to the measurement. Within the chamber, the 90%, 70% and the 50% contours are in agreement with the measurement. Outside the chamber, however, the convection of the current lines in the simulation is less than the measurement. This discrepancy could be due to the relatively higher magnetic Reynolds' number of the experimental case, or due to limitations of the continuum assumption (inherent in eqn.(1)) in the low collisionality region of the plume.

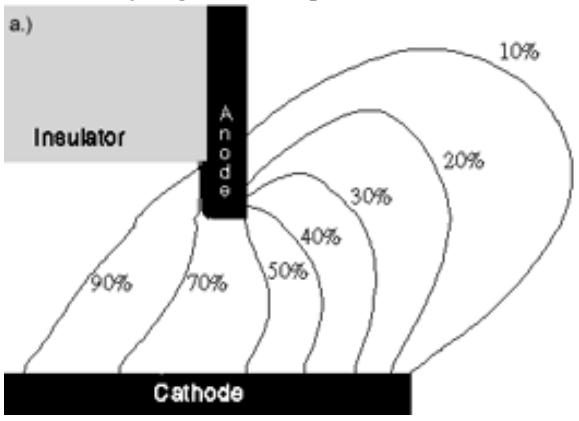

Figure 3: Calculated current contours for J = 16 kA.

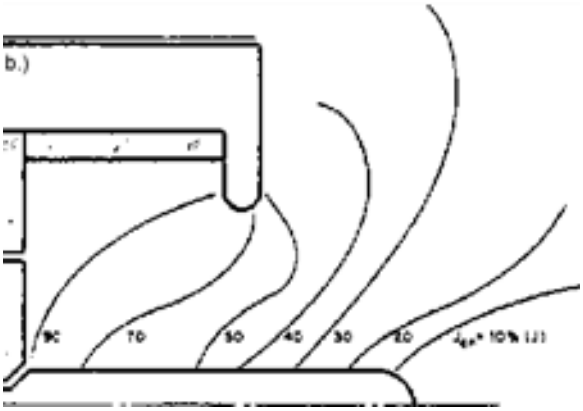

Figure 4: Measured current contours for J = 23.5 kA.

36 V, as shown in Fig.5. Because the simulation did not include fall voltages, we cannot compare to the measured total voltage drop[9] directly.

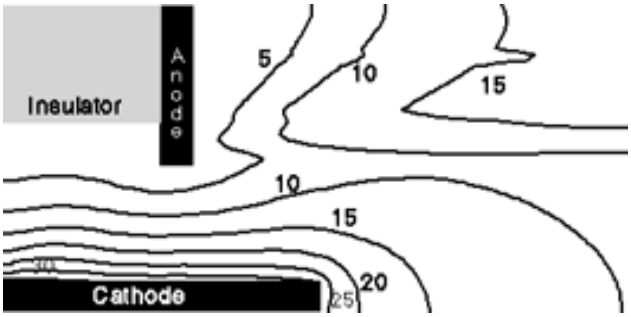

Figure 5: Calculated potential contours.

5.4 Temperatures

The calculated values of electron temperature are shown in Fig.14. In the bulk of the chamber, T_e ranges from 1.0 to 1.75 eV, which is in the range of measurements in ref.[27]. The rear top end of the chamber has lowest values (0.75 eV), because it has the lowest Ohmic-heating rate. The highest values of $\simeq 3.5$ eV are found on the inner and outer faces of the anode. This can be explained by the large Ohmic heating caused by the high current density observed in that region. Diamant[8] measured temperatures around 2.5 eV near the anode, those measurements are in general agreement with the simulation, in that region. Temperatures of $\simeq 3.0$ eV are seen in the simulation in front of the cathode on the centerline.

5.5 Thrust and Voltage

By definition, the thrust is computed using the following relation,

$$T = \int_A u_z \left(\rho \mathbf{u} \cdot d\mathbf{A}\right) \ . \tag{13}$$

Using eqn.(13), the code predicts a thrust of 51.2 N. For the FSBT at this operating condition (with a slightly different mass injection), the measured value of thrust was 50.4 N [9].

This simulation predicts a plasma voltage drop of

6 Insight into MPDT Physical Processes

As evident from the preceding section, this simulation has predicted many of the salient features of the flowfield, and the results are in general agreement with measurements for many quantities. Therefore, we can now use this simulation to delve into some of the physical mechanisms of the MPDT.

6.1 Effect of the Anode Lip

The velocity streamlines in the FSBT are shown in Fig.6. The expansion of the streamlines past the anode lip, and hence plume divergence, is evident from the figure. It is clear that the anode lip is an obstruction to the streamlines, and its stagnation effect can be seen in the increased density (Fig.11) and temperature (Fig.14) in that region.

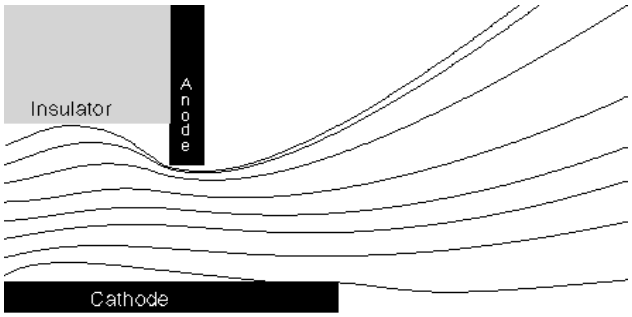

Figure 6: Calculated velocity streamlines.

In order to ascertain the effect of the anode lip on thrust, we need to look at the mass flux, and the momentum flux in this thruster.

Cory[28] measured the mass flux at this operating condition for the "Configuration A" thruster. The results of this simulation are compared to those measurements in Fig.7. Generally, the agreement between the simulation and the data is very good. Except for the point on the centerline, the agreement is within 20%. Near the centerline, the data predicts a higher mass flux than the simulation. This may be attributed to the difference in the cathode lengths in the experiment and the simulation.

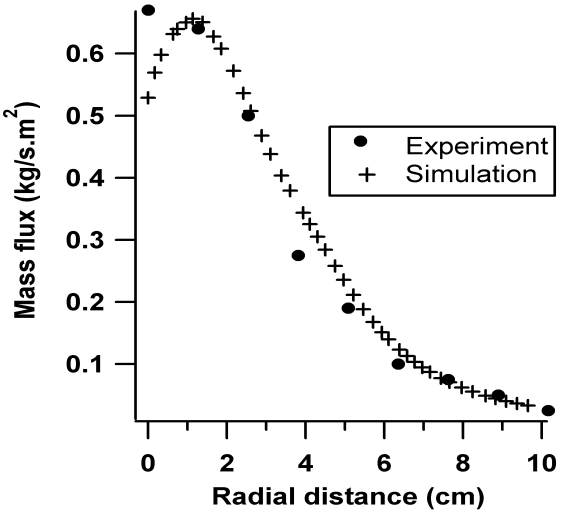

Figure 7: Mass flux at a distance of 12.5 cm from the anode plane. No error bars on the measurements were provided in the original work[28].

The flux of momentum was also calculated, and is shown in Fig.8.

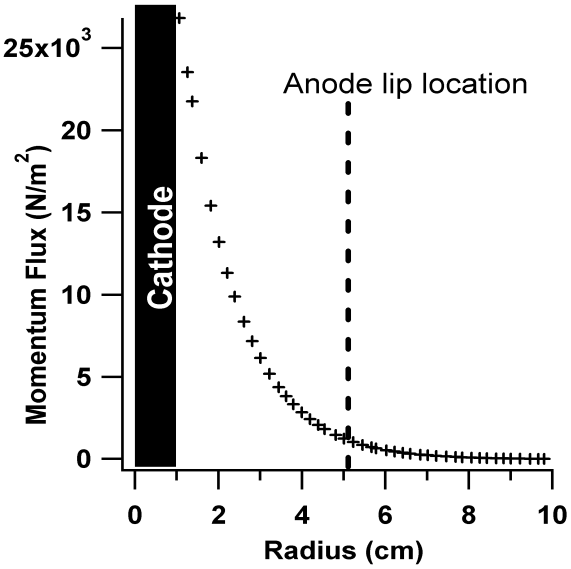

Figure 8: Calculated momentum flux at the cathode tip plane.

As seen in Fig.7, the flux of mass near the anode is relatively small. More importantly, as seen in Fig.8, the flux of momentum in the anode region is small compared to the cathode region. Due to a combination of the pumping force ($j_z B_\theta$) pushing the plasma towards the cathode, and the $1/r^2$ variation of the axial Lorentz force density ($j_r B_\theta$), the high speed jet is confined to the cathode region of the thruster, and the anode region does not play a significant role in the momentum flux. Therefore, the anode lip is not a significant impediment to the production of thrust.

6.2 Ionization Levels

The effective ionization fraction is shown in Fig.15. It is important to bear in mind that this simulation uses an equilibrium ionization model, and hence $Z = Z(n, T_e)$, and therefore an understanding of T_e distribution is important to understand the distribution of ionization levels. In the rear top end of the chamber, where the current density is low ($\simeq 5.0 \times 10^4$A/m^2), we find that the ionization level is low ($Z \simeq 0.25$), as expected. In the bulk of the chamber, $Z \simeq 1.0$. Near the inner face of the anode

and the anode lip, where the current density is high, the effective ionization level ranges from 1.5 to 2.5. In the outer edge of the anode, current density is also very high, the ionization level is $\simeq 3.0$. The presence of these higher states of ionization (Ar-III and Ar-IV) has been shown by Bruckner[18] in the anode plane of the "Configuration A" thruster, for these operating conditions (argon at 6.0 g/s, J=16.0 kA).

6.3 Cathode Barrel

In many experimental observations[1, 29] at nominal operating conditions, the luminous structure of the discharge was observed to have some invariant features, such as a "cathode jet", a luminous barrel which is larger at the base of the cathode and constricts towards the middle and expands again at the cathode tip. All of these features can be seen in Fig.16. On the left panel of Fig.16 are the calculated values electron density, which can be qualitatively related to the light emission from the discharge shown on the right panel.

6.4 Current on the Cathode

The current distribution on the cathode is shown in Fig.9. Near the inlet, the surface current density has a value of $\simeq 550$A/cm^2, and quickly decreases to $\simeq 200$A/cm^2 along most of the cathode, only to rise again near its tip. This is compared with the measurements by Boyle[26] who measured similar values along the cathode, in Fig.9. However, while ref.[26] reports that the current density at the cathode tip is in excess of 1000A/cm^2, the simulation only predicts $\simeq 550$A/cm^2. This difference could be because the cathode in ref.[26] was shorter than that of the FSBT, and had a conical tip, as opposed to the hemispherical tip of the FSBT. As seen in Fig.9, the longer cathode (simulation) has a greater surface area, and hence lesser current density. This may play a role in reducing erosion, as well as in decreasing Ohmic dissipation (to be discussed below).

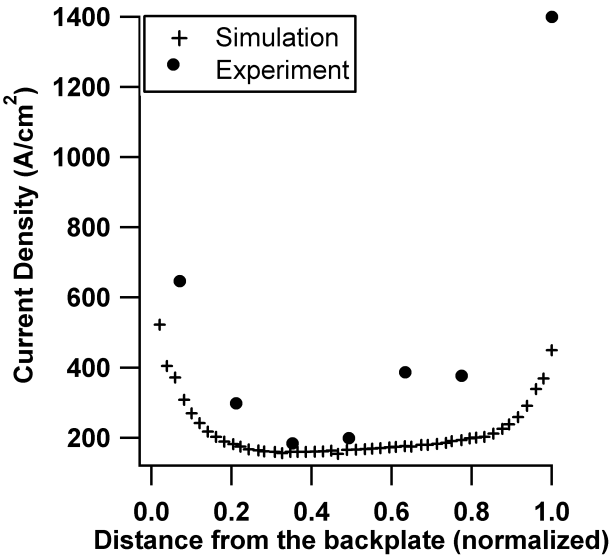

Figure 9: Surface current density on the cathode. Error bars on the measurement are not available in the original source[26].

6.5 Thrust Composition

As mentioned earlier, the simulation predicted a thrust of 51.2 N, compared to the measured value of 50.4 N. We can compute the electromagnetic contribution to the thrust to be

$$T_{EM} = \int (\mathbf{j} \times \mathbf{B}) dV. \qquad (14)$$

For the case under consideration, the electromagnetic component was 38.0 N, which is 75% of the total thrust. This implies that at this regime of operation (argon at 6.0 g/s, J = 16.0 kA), the FSBT is predominantly an electromagnetic accelerator.

6.6 Energy Deposition

The total power deposited into the MPDT plasma can be split into kinetic power and dissipation,

$$\int \mathbf{j} \cdot \mathbf{E} dV = \int (\mathbf{j} \times \mathbf{B}) \cdot \mathbf{u} dV + \int \eta j^2 dV. \quad (15)$$

The second term on the right hand side is often termed the "dissipation integral"[30, 31], and under-

standing and quantifying it is essential to improving the efficiency of the MPDT. We have calculated all the three terms in eqn.(15) for the FSBT, and the results are shown in Fig.10.

In a coaxial configuration, the current density is inversely proportional to the radius, and therefore the power deposition, and the dissipation, are large near the cathode. This is evident in Fig.10, where almost 45% of the dissipation occurs in the "inner flow" region[26] which is restricted to 1 cm around the cathode. As with thrust production (cf. §6.1), this near cathode region is an important one in energetics as well. For consistency, one can verify that the sum of all the input power in all the zones in Fig.10 add up to VJ (571 kW).

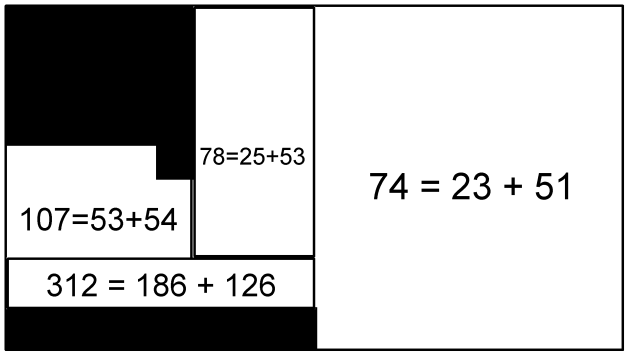

Figure 10: Power expenditure in various regions (kW). The values of each of the terms in eqn.(15) are shown in various regions.

It is worth noting that the shell near the cathode is the only region where the kinetic power exceeds the Ohmic heating, which is largely unrecovered.

7 Concluding Remarks

We have described the reformulation of our MHD code that was developed for the simulation of propulsive plasma flows. We presented the physical models: the two-temperature MHD equations with suitable transport properties, ionization and equation of state models. We also discussed the techniques for obtaining a numerical solution of the governing equations.

The code was used to simulate plasma flows in the Princeton full-scale benchmark thruster. The calculated contours of density, ionization levels, velocity, mass flux patterns, enclosed current contours, cathode surface current density, and temperature compared well with measurements at similar operating conditions. The calculated value of thrust matched with the measured value within 2%.

The code was then used to provide insight into some physical mechanisms. Among the important observations are:

- Despite being a cause of stagnation in a part of the flow, the anode lip does not have a serious adverse effect on the thrust.
- The FSBT is predominantly an electromagnetic accelerator at its nominal operating condition (J=16 kA, $\dot{m}$ = 6.0 g/s of argon).
- The "inner flow" region 1 cm around the cathode plays an important role in the energetics.

Currently, this code is being utilized to simulate the operation of the FSBT at other regimes of operation. Convergence problems at higher current levels are being addressed. The next goal of this effort is to simulate the performance of other thrusters, such as the LiLFA, for which there is a dearth of data.

References

[1] L. K. Rudolph. *The MPD Thruster Onset Current Performance Limitation*. PhD thesis, Princeton U., 1980.

[2] D. D. Ho. Erosion Studies in a (MPD) Thruster. Master's thesis, Princeton U., 1981.

[3] D. I. Kaplan. Performance Chatacteristics of Geometrically-Scaled Magnetoplasmadynamic (MPD) Thrusters. Master's thesis, Princeton U., 1982.

[4] M. J. Wolff. A High Performance Magnetoplasmadynamic Thruster. Master's thesis, Princeton University, 1984.

[5] J. H. Gilland. The Effect of Geometric Scale upon MPD Thruster Behavior. Master's thesis, Princeton University, 1988.

[6] W. A. Hoskins. Asymmetric Discharge Patterns in the MPD Thruster. Master's thesis, Princeton University, 1990.

[7] A. D. Gallimore. *Anode Power Deposition in Coaxial MPD Thrusters*. PhD thesis, Princeton U., 1992.

[8] K. D. Diamant. *The Anode Fall in a High Power Pulsed MPD Thruster*. PhD thesis, Princeton U., 1996.

[9] E.Y. Choueiri and J.K. Ziemer. Quasi-Steady Magnetoplasmadynamic Thruster Performance Database. *Journal of Propulsion and Power*, 17:967–976, 2001. September-October.

[10] K. Sankaran, L. Martinelli, S.C. Jardin, and E.Y. Choueiri. A flux-limited numerical method for the MHD equations to simulate propulsive plasma flows. *Int. J. Num. Meth. Eng.*, 35, #5, 2002.

[11] K. Sankaran, E.Y. Choueiri, and S.C. Jardin. Application of a new numerical solver to the simulation of MPD flows. *AIAA-2000-3537*, 2000.

[12] K. Sankaran, S.C. Jardin, and E.Y. Choueiri. Parallelization and validation of an MHD code for the simulation of self-field MPDT flows. *IEPC-01-127*, 2001.

[13] V.P. Ageyev and V.G. Ostrovsky. High-current stationary plasma accelerator of high power. In *Proceedings of the 23rd International Electric Propulsion Conference*, Seattle, WA, USA, 1993. IEPC-93-117.

[14] E.Y. Choueiri. Anomalous resistivity and heating in current-driven plasma thrusters. *Phys. Plasmas*, 6(5):2290, 1999.

[15] E.Y. Choueiri. Instability of a current-carrying finite-beta collisional plasma. *Phys. Review E*, 64(6), 2001.

[16] E. J. Sheppard. *Ionization Nonequilibrium and Ignition in Self-Field Magnetoplasmadynamic Thrusters*. PhD thesis, MIT, 1992.

[17] E. H. Niewood. *An Explanation for Anode Voltage Drops in an MPD*. PhD thesis, MIT, 1993.

[18] A. P. Bruckner. *Spectroscopic Studies of the Exhaust Plume of a Quasi-Steady MPD Accelerator*. PhD thesis, Princeton U., 1972.

[19] T. M. Randolph. Measurement of Ionization Levels in the Interelectrode Region of an MPD Thruster. Master's thesis, Princeton University, 1994.

[20] H. O. Schrade, P. C. Sleziona, T. Wegmann, and H. L. Kurtz. Basic processes of plasma propulsion: Final report. *AFOSR: 91-0118*, 1991.

[21] M.R. LaPointe and P.G. Mikellides. High Power MPD Thruster Development at the NASA Glenn Research Center. *AIAA-01-3499*, 2001.

[22] E.Y. Choueiri and H. Okuda. Anomalous ionization in MPD thrusters. *IEPC-93-067*, 1993.

[23] E.Y. Choueiri. The scaling of thrust in self-field MPD thrusters. *J. Prop. Power*, 14(5):744–753, 1998.

[24] P. J. Turchi and R. G. Jahn. Cathode Region of a Quasi-Steady MPD Arcjet. *AIAA J.*, 9(7), 1971.

[25] A. J. Kelly and R. G. Jahn. Pulsed electromagnetic acceleration: JPL contract no.954997. *MAE Report*, 1692.23, 1986.

[26] M. J. Boyle. *Acceleration Processes in the Quasi-Steady Magnetoplasmadynamic Discharge*. PhD thesis, Princeton U., 1974.

[27] P. J. Turchi. *The Cathode Region of a Quasi-Steady Magnetoplasmadynamic Arcjet*. PhD thesis, Princeton U., 1970.

[28] M. S. DiCapua. *Mass, Momentum and Energy Flow from an MPD Accelerator*. PhD thesis, Princeton U., 1971.

[29] R. G. Jahn, W. F. von Jaskowsky, and K. E. Clark. Pulsed electromagnetic acceleration. *MAE Report*, 1467a, 1979.

[30] D. D. Villani. *Energy Loss Mechanisms in a Magnetoplasmadynamic Arcjet*. PhD thesis, Princeton U., 1982.

[31] E. Y. Choueiri. *Advanced Problems in Plasma Propulsion*. Princeton U. Lecture Notes, 1998.

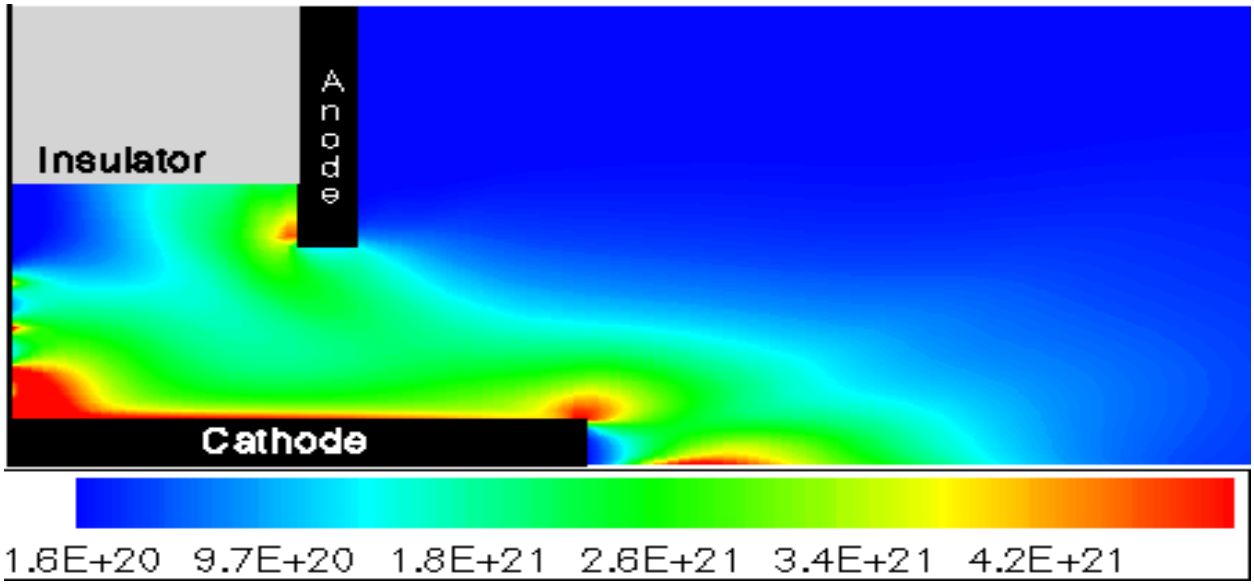

Figure 11: Calculated electron number density (m^{-3})

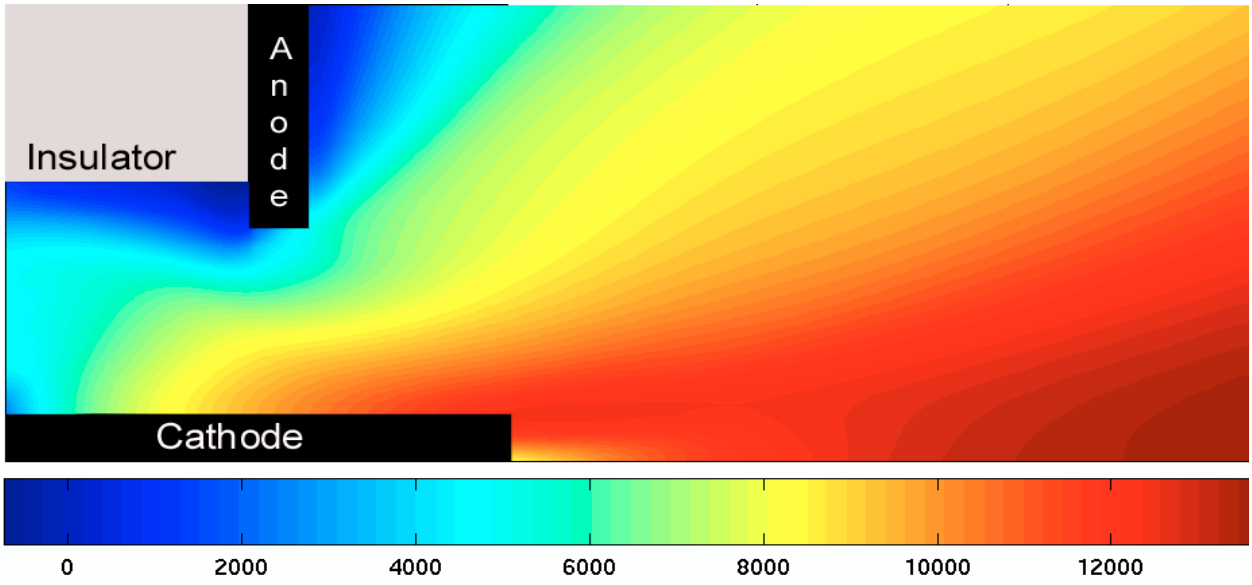

Figure 12: Calculated axial velocity (m/s)

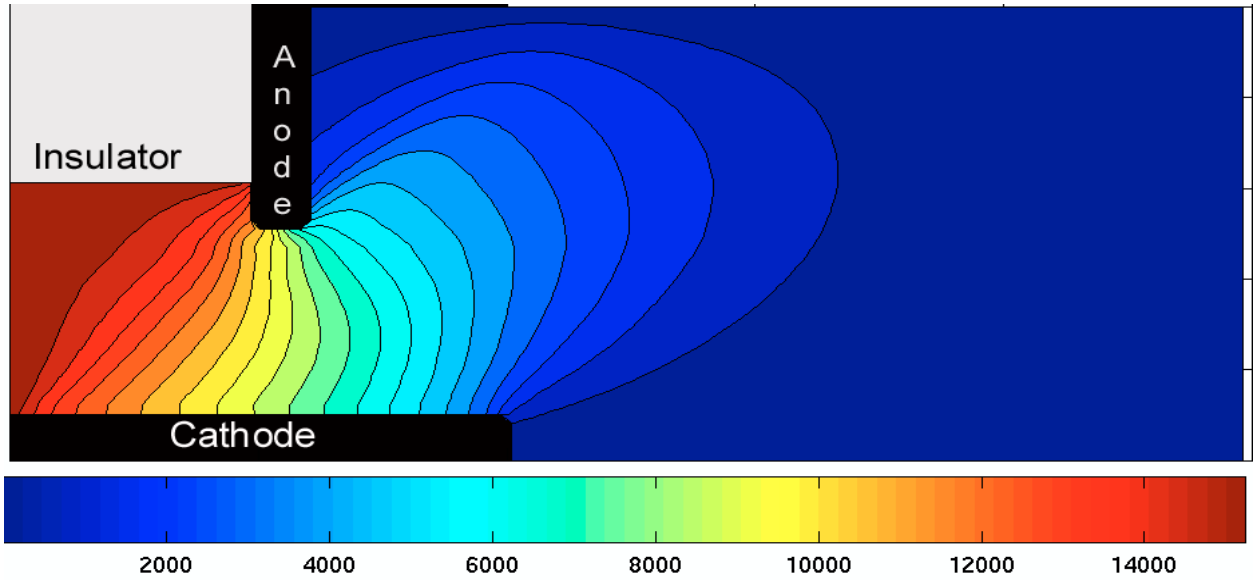

Figure 13: Calculated enclosed current contours (1000 A between each)

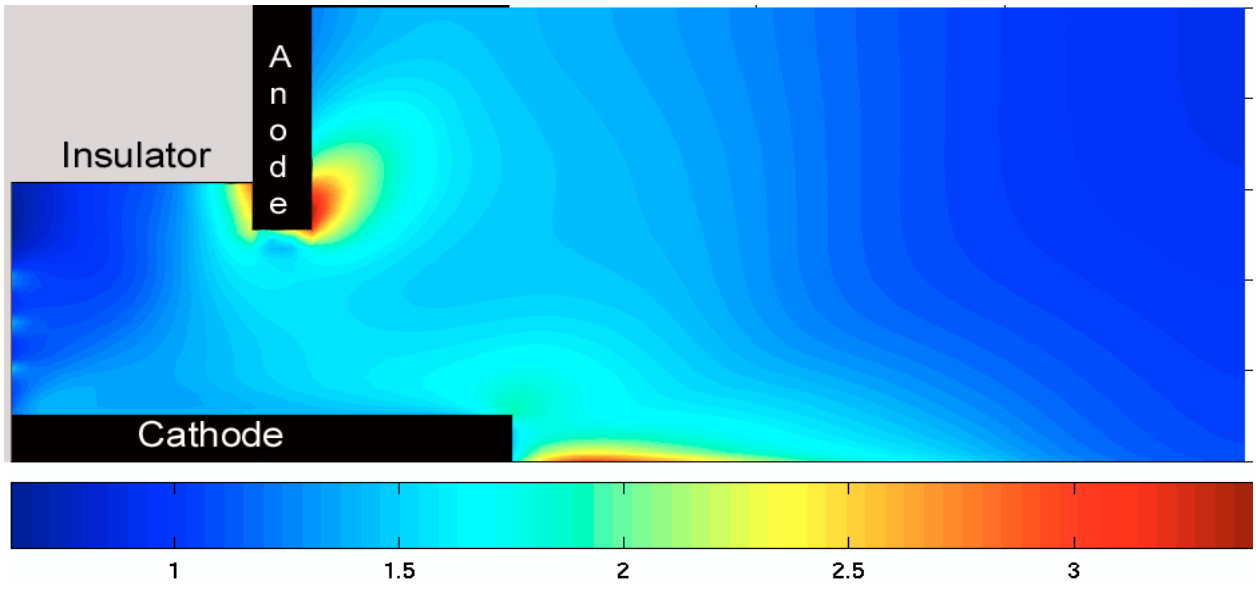

Figure 14: Calculated electron temperature (eV)

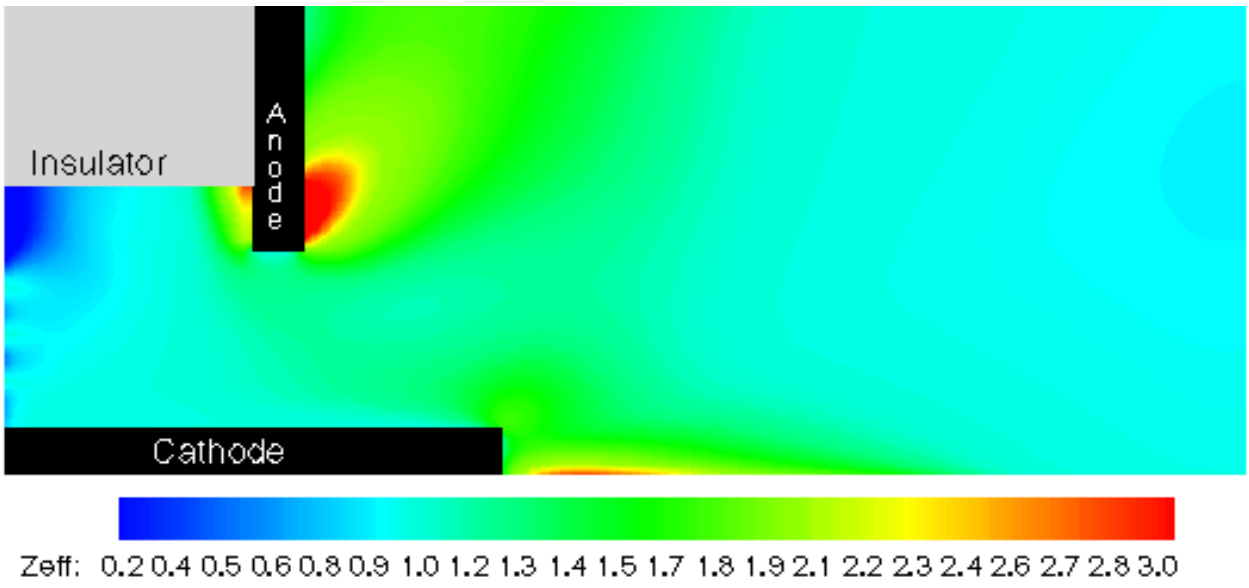

Figure 15: Calculated effective ionization fraction

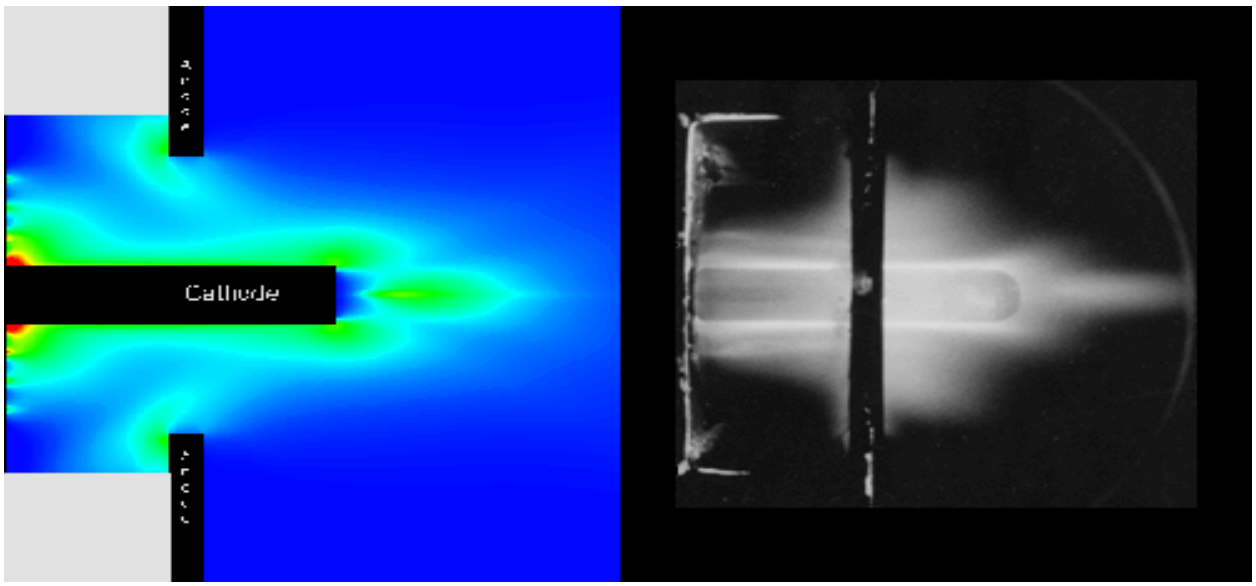

Figure 16: Left: Calculated electron number density (m^{-3}); Right: Photographs of light emission from FSBT discharge with transparent walls[29]

A Governing Equations

So, the finite volume formulation of eqn.(1) is,

$$\frac{\partial}{\partial t}\begin{bmatrix} r\rho \\ r\rho u \\ r\rho w \\ B_\theta \\ r\mathcal{E} \end{bmatrix} = \frac{\partial}{\partial r}\begin{bmatrix} -r\rho u \\ -r\left(\rho u^2 + p + \frac{B^2}{2\mu_o}\right) \\ -r\rho uw \\ E'_z - uB_\theta \\ -r\left(u\left(\mathcal{E} + p + \frac{B^2}{2\mu_o}\right) - q_r\right) \end{bmatrix} + \frac{\partial}{\partial z}\begin{bmatrix} -r\rho w \\ -r\rho uw \\ -r\left(\rho w^2 + p + \frac{B^2}{2\mu_o}\right) \\ -\left(E'_r + wB_\theta\right) \\ -r\left(w\left(\mathcal{E} + p + \frac{B^2}{2\mu_o}\right) - q_z\right) \end{bmatrix} + \begin{bmatrix} 0 \\ p - B^2/(2\mu_o) \\ 0 \\ 0 \\ 0 \end{bmatrix} . \tag{16}$$

B Derivatives in Non-orthogonal Coordinates

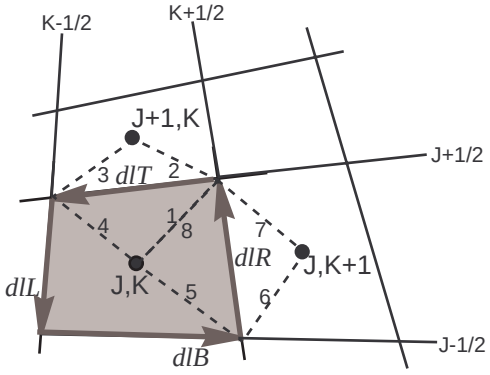

Figure 17: A general non-orthogonal control volume.

Recall that, if some vector $\hat{\mathbf{B}} = [0, -rB]$, then,

$$\nabla \times \hat{\mathbf{B}} = \frac{\partial (rB)}{\partial r} . \tag{17}$$

Using Stokes' theorem, this becomes,

$$j_z = \frac{1}{\mu_o}\frac{1}{r}\frac{\partial (rB)}{\partial r} = \frac{1}{\mu_o}\frac{1}{r}\frac{1}{A[J+\frac{1}{2}][K]}\oint [0, -rB]\cdot \mathbf{dl} . \tag{18}$$

Similarly, if $\hat{\mathbf{B}} = [B, 0]$, then,

$$\nabla \times \hat{\mathbf{B}} = \frac{\partial B}{\partial z} , \tag{19}$$

which becomes,

$$j_r = -\frac{1}{\mu_o}\frac{\partial B}{\partial z} = -\frac{1}{\mu_o}\frac{1}{A[J][K+\frac{1}{2}]}\oint [B,0]\cdot \mathbf{dl}\ . \tag{20}$$

Here, $A[J][K+\frac{1}{2}]$ and $A[J+\frac{1}{2}][K]$ refer to the areas of the dotted cells in Fig.17 to the right and top, respectively. They can be estimated a simple averages of the control volumes.

The contour integrals in eqns.(20,18) require estimation of B along **dl**, which is the dotted line in Fig.17. First, the line element vectors, **dl**, themselves have to be computed from the coordinates of the vertices and the center of the cell. Then, B along this line element can be obtained by averaging from the nearby cell centers.